Soft Matter

PAPER

View Article Online
View Journal | View Issue

Cite this: *Soft Matter*, 2025, **21**, 8510

Dynamics of the antiferroelectric smectic-Z_A phase in a ferroelectric nematic liquid crystal

Arjun Ghimire,[a] Bijaya Basnet,[b] Hao Wang,[b] Parikshit Guragain,[c] Alan Baldwin,[a] Robert Twieg,[c] Oleg D. Lavrentovich,[ab] James Gleeson,[a] Antal Jakli[ab] and Samuel Sprunt*[ab]

Received 4th August 2025,
Accepted 16th October 2025

DOI: 10.1039/d5sm00796h

rsc.li/soft-matter-journal

A dynamic light scattering study of director fluctuations in the antiferroelectric (AF) phase of the ferroelectric nematic liquid crystal DIO is reported. The AF phase occurs in a temperature range between nonpolar (paraelectric) and ferroelectric nematic states. The behavior of the observed fluctuation modes is consistent with the smectic-Z_A model of the AF phase – namely, a smectic layer structure defined by fluid layers of alternating electric polarization, with the polarization field and nematic director both oriented parallel to the layer planes. This model has been advanced to explain a large body of previous experimental results on DIO. We discuss the wave vector dependence of the modes in terms of a dynamical theory based on the elastic free energy density of a smectic-C phase in the limit of 90° director tilt and an approximation of the viscous stresses by their form for an incompressible uniaxial fluid. We also present the pretransitional temperature dependencies of the splay, twist, and bend elastic constants and the corresponding viscosities in the paraelectric nematic phase.

1 Introduction

The discovery of a spontaneously ferroelectric nematic phase in highly polar liquid crystals[1–4] – anticipated over a century ago by Born[5] – is certainly one of the most exciting recent developments in soft materials science. Since 2020, there has been an explosion in the synthesis and physical characterization of ferroelectric nematic compounds, many based on the original molecular architectures or mixtures thereof[6–11] and others representing distinct new types.[12–15] In these materials, the ferroelectric polarization typically develops at temperatures below a conventional (paraelectric) nematic phase, although it may also form *via* direct transition from the isotropic state.[13,16] The polarization field $\vec{P}$ coincides with the average direction of the molecular long axis (nematic director $\hat{n}$), and the magnitude of $\vec{P}$ reaches values corresponding to nearly perfect alignment of the molecular dipoles.

Remarkably, the ferroelectric nematic is only one member of an expanding "realm" of related ferroelectric and antiferroelectric phases,[17–24] including smectic phases exhibiting polar layer structures. Of particular interest is an antiferroelectric (AF) phase, first reported in the compound DIO,[1] that occurs in a temperature range between the paraelectric and ferroelectric nematic states. In DIO, resonant carbon K-edge and off-resonant X-ray scattering, combined with measurements of polarization current under an AC electric field, reveal the alternating polarization field has period 18 nm and is accompanied by a mass density wave with half this period.[19] The density wave (wave vector $\vec{q}_0$) and polarization modulation are parallel to each other, and their direction is normal to the average $\vec{P}$ and $\hat{n}$ in each layer.

These observations led to the identification of the intermediate phase in DIO as a new smectic phase, designated smectic-Z_A, where "Z" denotes the opposite extreme from a smectic-A phase with respect to the tilt angle between $\hat{n}$ and the layer normal (90° in the smectic-Z_A *vs.* 0° in the smectic-A), and "A" indicates AF ordering along the layer normal. The X-ray data also showed a temperature-dependent decrease in layer spacing on cooling below the nematic. In thin, planar optical cells treated for homogeneous alignment of $\hat{n}$, the layer contraction produces distinctive textures[19] indicative of the chevron layer structure originally described in surface-stabilized ferroelectric smectic-C liquid crystals near the C to A transition.[25] Similar chevron textures were also observed in the intermediate phase in mixtures of DIO with a different polar nematic compound.[20]

However, experimental results on another prototypical ferroelectric nematic compound, RM734,[2] and particularly its mixture with ionic liquids,[26] suggest an alternative structure for the intermediate phase. In pure RM734, the onset of polar order is

[a] *Department of Physics, Kent State University, Kent, OH 44242, USA. E-mail: ssprunt@kent.edu*
[b] *Materials Science Graduate Program and Advanced Materials and Liquid Crystal Institute, Kent State University, Kent, OH 44242, USA*
[c] *Department of Chemistry, Kent State University, Kent, OH 44242, USA*

preceded by a dramatic decrease with temperature of the elastic constant and relaxation rate associated with splay director fluctuations.[27] When doped with ionic additives, the temperature range of a very narrow AF phase below the paraelectric nematic expands significantly, and the doped system exhibits an optical stripe texture, with the stripes running parallel to $\vec{P}$.[26] Combined polarizing optical and second harmonic generation microscopy revealed evidence of a 2D splay-modulated phase, designated N_{S_2}, with optical scale periodicity. Periodic reversal in sign of director splay $\left(\vec{\nabla}\cdot\hat{n}\right)$ enables the splay structure to fill space, and the accompanying reversal of $\vec{P}$ accounts for the AF response to an applied electric field. Additional evidence of a N_{S_2} phase has been reported in RM734 samples confined in thin planar cells coated with a cationic polymer.[28] One- and two-dimensional splay-modulated phases have also been studied theoretically for highly polar liquid crystals.[29,30]

The splay-modulated and smectic-Z_A models are not necessarily incompatible. For instance, in a 1D splay-modulated phase (N_{S_1} phase), the reversal in $\nabla\cdot\hat{n}$ and $\vec{P}$ may coincide with a one-dimensional density variation proportional to P^2 (with half the period of the AF order), as suggested in ref. 26. Also, in different ferroelectric nematic materials, splay modulation might develop with substantially shorter period than an optical wavelength. And if the concentration of free ions is relatively low, this modulation might be weak due to high electrostatic energy cost associated with the accompanying polarization splay and accumulation of bound charge. The N_{S_1} and smectic-Z_A models would then possess similar physical characteristics.

In this paper, we report a dynamic light scattering study of the orientational fluctuation modes in the paraelectric nematic and lower temperature AF phase of DIO. We analyze the results for the latter in terms of a dynamical model for the smectic-Z_A phase based on a combination of the elastic free energy for a smectic-C,[31] in the limit of 90° tilt angle, with the hydrodynamic equations for an incompressible uniaxial fluid. (As a "first order" approximation, we neglect complications of the viscous stresses due to biaxiality of the smectic-Z_A layer structure).

We find that the model accounts reasonably well for the behavior of the observed overdamped fluctuation modes. In particular, the continuous temperature dependence of the amplitude and relaxation rate of director bend fluctuations confirms perpendicular orientation of the director relative to the smectic density wave, just as the continuity of these quantities for splay fluctuations across a nematic to ordinary smectic-A transition reflects a parallel orientation. The wave vector ($\vec{q}$) dependence of the measured relaxation rates are also broadly consistent with the model, although quantitative comparison with the data reveals some limitations. Additionally, we present the pretransitional behavior of splay, twist, and bend elasticities and viscosities in the nematic phase of DIO and compare them with previously reported measurements on the compound RM734.[27]

Based on the body of available experimental results, we shall hereafter refer to the AF phase in DIO as a smectic-Z_A ("Sm Z_A") phase.

2 Experimental details

Dynamic light scattering and simultaneous polarizing optical microscopy were performed on a 20 μm thick sample of purified *trans* DIO contained between planar optical substrates. The inner substrate surfaces were treated with rubbed polyimide alignment layers, and the cell was assembled with the rubbing directions on the two surfaces oriented parallel to each other (*syn*-parallel alignment) in order to produce homogeneous planar orientation of the average director $\hat{n}_0$. The outer cell surfaces were coated with an anti-reflection coating designed for the visible range. The sample cell was housed in a temperature-regulated hot stage, which has ±50° optical access for scattered light and typical temperature stability of 0.01 °C. The hot stage was mounted on a goniometer that allowed independent control of the incident and scattering angles. These angles are defined in the horizontal scattering plane and measured relative to the normal to the vertical sample plane. An additional rotation stage enabled variation of the nematic director orientation relative to the scattering plane.

The two scattering geometries used are summarized in Fig. 1. In the nematic phase, they correspond to the twist-bend mode of the director when $\hat{n}_0$ lies in the scattering plane (Geometry 1) or to a combination of pure splay and pure twist director fluctuations when $\hat{n}_0$ is perpendicular to the scattering plane (Geometry 2). In both cases, the polarization of normally incident laser light (wave vector $\vec{k}_i$, with $|\vec{k}_i| = k_0 = 2\pi/532\ \mathrm{nm}^{-1}$) was set perpendicular to $\hat{n}_0$, and the maximum intensity of the focused beam at the sample was 0.1 W mm^{-2}.

The depolarized scattered light intensity $I_s(t)$ and the temporal intensity correlation function, $g^{(2)}(\tau) = \dfrac{\langle I_s(t)I_s(t+\tau)\rangle}{\langle I_s(t)\rangle^2}$ (where the angled brackets represent a time average), were recorded at various temperatures on cooling and for scattering angles θ_s ranging from 2.5° to 50° at each temperature in the two scattering geometries. In terms of θ_s, the components of the scattering vector $\vec{q} = \vec{k}_s - \vec{k}_i$ are

$$q_y = 0,\ q_z = k_0 \sin\theta_s,\ q_x = k_0\left(n_\parallel\sqrt{1-\frac{\sin^2\theta_s}{{n_\perp}^2}} - n_\perp\right) \quad (1a)$$

in Geometry 1 and

$$q_z = 0,\ q_y = k_0 \sin\theta_s,\ q_x = k_0\left(\sqrt{{n_\parallel}^2 - \sin^2\theta_s} - n_\perp\right) \quad (1b)$$

in Geometry 2. Here $n_{\perp(\parallel)}$ is the refractive index for polarization perpendicular (parallel) to $\hat{n}_0$, and we have neglected the small optical biaxiality measured in the Sm Z_A phase.[19] Representative examples of the measured correlation function $g^{(2)}(\tau)$ in the nematic and Sm Z_A phases are presented in Fig. S1 and S2.

In a typical experimental run, the sample was heated from room temperature to 120 °C in the nematic phase, ~36 °C above the transition to the Sm Z_A phase (temperature T_{NZA}) and ~56 °C below the transition to the isotropic phase. Excellent homogeneous planar alignment of the director was confirmed by *in situ* polarizing optical microscopy (POM) in both the

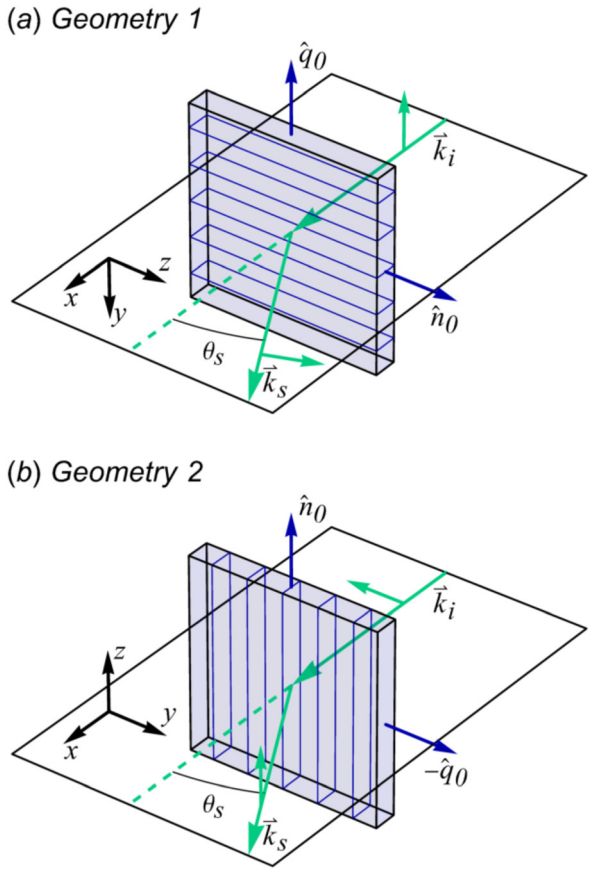

Fig. 1 Depolarized light scattering geometries used in this study. The equilibrium director ($\hat{n}_0 = \hat{z}$) coincides with the substrate rubbing direction and is oriented parallel (Geometry 1, (a)) or perpendicular (Geometry 2, (b)) to the scattering plane. Wave vectors of the normally incident laser beam ($\vec{k}_i$) and the scattered light ($\vec{k}_s$, collected at lab angles $\theta_s = 2.5–50^\circ$ from the normal), are shown in green, together with their polarizations. Blue outlines indicate the layer structure associated with the Sm Z_A phase. The layers are shown in the "bookshelf" geometry with layer normal indicated by $\hat{q}_0$, which is also the direction of the polarization modulation.

nematic and SmZ_A phases (Fig. S3(a)–(c)). From observation of the POM texture and an abrupt decrease in splay scattering intensity, we determined $T_{NZA} \approx 84.25$ °C in our sample. In order to avoid thermal *trans–cis* isomerization of the DIO molecules, the sample was not heated above 120 °C. Contamination by the *cis* stereoisomer strongly suppresses the Sm Z_A phase,[32] but no evidence of this was seen during our experiments.

Previous studies[19,33] reveal that in thin cells with parallel surface alignment layers and in the absence of applied bulk fields, the layer structure defined by the mass density wave in the Sm Z_A phase forms in the "bookshelf" geometry on cooling from the nematic. At the transition, the layer planes develop normally to the cell surfaces, as depicted in Fig. 1.

To confirm the bookshelf layer orientation, we studied the twist Freedericksz transition in samples of DIO treated with similar planar alignment layers.[34] In the nematic phase, we clearly observed induced director reorientation under an in-plane electric field applied across a 1 mm gap. In the Sm Z_A phase, domains with smectic layers and director both parallel to the cell surfaces should offer no additional resistance to twist, and the Freedericksz transition should be readily observable at field levels comparable to the threshold field for the nematic phase. Instead, after cooling just below T_{NZA} in zero field, no twist transition was observed as the field was ramped through the nematic threshold. This indicates the bookshelf layer orientation, since in that case the field-induced twist would be strongly resisted by the layer structure. As described in Section 4, our light scattering results also corroborate the bookshelf geometry.

3 Results

3.1 Inverse scattered intensity and orientational elastic constants

The intensity scattered from director fluctuations is proportional to the mean square Fourier component of the fluctuating dielectric tensor picked out by the choice of incident (i) and scattered (s) light polarizations at the scattering vector $\vec{q}$: $I_s(\vec{q}) \propto \left\langle \left| \hat{s} \cdot \delta\vec{\vec{\varepsilon}}(\vec{q}) \cdot \hat{i} \right|^2 \right\rangle$. This quantity scales with the square of the dielectric constant anisotropy, $\Delta\varepsilon = \varepsilon_0(n_\parallel{}^2 - n_\perp{}^2)$ (for a uniaxial medium), and with q^{-2} (for hydrodynamic director modes). We therefore consider $I_n(\vec{q}) = \left(\frac{\varepsilon_0}{\Delta\varepsilon}\right)^2 \frac{q^2}{k_0{}^2} \frac{P_{ref}}{P} \frac{1}{T_{sc}} I_s(\vec{q})$, which normalizes I_s for variation of $\Delta\varepsilon$ with temperature, magnitude of $\vec{q}$ selected, laser power P (P_{ref} being a fixed reference power), and transmittance T_{sc} of scattered light through the optical cell substrate. To calculate $\Delta\varepsilon$, we used values of $n_\perp$ and $n_\parallel$ as a function of temperature measured by a wedge cell technique[35] at 532 nm wavelength.

In Fig. 2, we plot the temperature dependence of the inverse normalized intensity $I_n{}^{-1}$ measured at lab scattering angles $\theta_s = 45^\circ$ and 2.5° in Geometry 2, and $\theta_s = 42.5^\circ$ in Geometry 1. In the nematic phase, these choices isolate scattering from essentially pure splay, twist, and bend director fluctuations, respectively

The blue points in Fig. 2 reveal that the inverse scattered intensity $I_n{}^{-1}$ for nematic bend fluctuations (with wavevector $\vec{q}$ parallel to the average director) is continuous across the transition to the Sm Z_A phase and weakly increasing with decreasing temperature on both sides of the transition. Apparently, the mass density wave (and accompanying AF order) have no significant impact on the scattering amplitude from director bend fluctuations. On the other hand, $I_n{}^{-1}$ for splay and twist fluctuations (orange and green points in Fig. 2) increases abruptly at the transition by $\sim$100 times. Below the transition, $I_n{}^{-1}$ exhibits a local minimum in the middle of the Sm Z_A phase. As we will discuss in Section IV below, the behavior of $I_n{}^{-1}$ for each scattering geometry can be explained by a Sm Z_A layer structure that develops in the bookshelf geometry.

Results for the orientational elastic constants in the nematic phase are plotted against temperature in Fig. 3. They are related to the scattered intensity by the expression,[36]

$$I_{s,\alpha}(\vec{q}) = CPT_{sc}\frac{k_B T(\Delta\varepsilon)^2 G_\alpha}{K_\alpha q_\alpha{}^2},$$

where $\alpha = 1, 2, 3$, K_1, K_2, and K_3 are the orientational (Frank) elastic

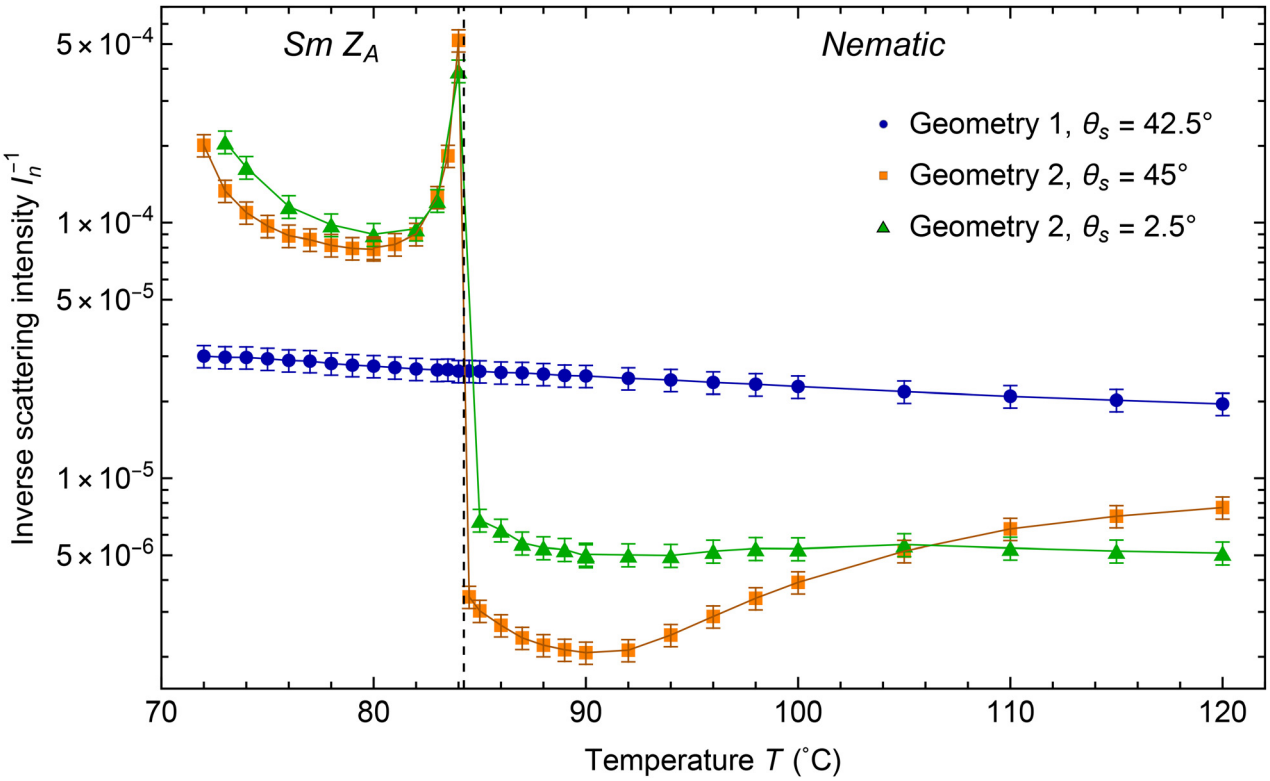

Fig. 2 Normalized inverse scattered light intensity *vs.* temperature measured on DIO in scattering geometries that correspond to pure bend, splay, and twist director fluctuations in the nematic phase (blue, orange, and green points, respectively). The dashed vertical line indicates the nematic to Sm Z_A transition temperature ($T_{NZA} \approx 84.25$ °C). As discussed in Section IV of the text, the presence of a smectic-like layer structure with layer normal along the modulation direction in the Sm Z_A phase couples director splay and twist fluctuations in Geometry 2. Solid lines are guides to the eye.

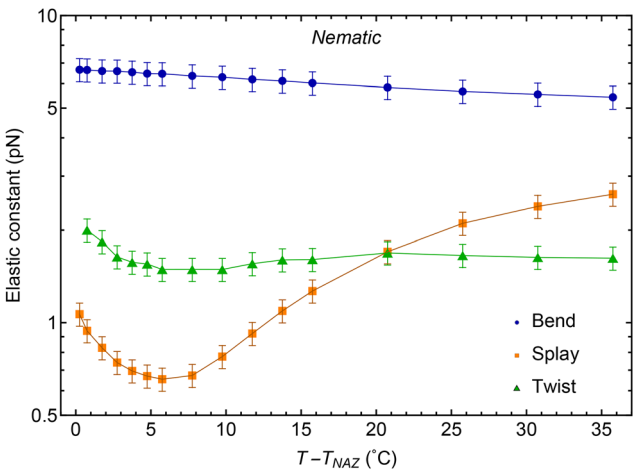

Fig. 3 Elastic constants for splay, twist and bend director distortions in the nematic phase of DIO, plotted *vs.* temperature relative to the nematic to Sm Z_A transition. Solid lines are guides to the eye.

constants for splay, twist, and bend director distortions, respectively, $G_\alpha = G_\alpha(n_\perp, n_\parallel, \theta_s)$ are factors determined from the selection of director fluctuations that contribute in each scattering geometry, and T is the absolute temperature. P is the incident laser power, and the prefactor C depends on the illuminated sample volume, the detection optics, and the photomultiplier tube and pulse amplification/discrimination instrumentation, all of which were maintained under precisely the same conditions during our measurements. We estimate that C was constant within 5% during our measurements.

Since P, T_{sc}, $\Delta\varepsilon$, T, G_α, and q_α were measured, or calculated using measured values of $n_\perp$, $n_\parallel$, the temperature dependence of the elastic constants K_α in the nematic phase may be determined from measurements of the intensities combined with an independent measurement of the absolute value of one of the K_α at a reference temperature. We used $K_1 = 1.1$ pN obtained from the electric field-induced splay Freedericksz transition in DIO at $T = 98$ °C.[37] Measurements above the Freedericksz threshold also yield the ratio of bend to splay constants $\frac{K_3}{K_1}$. We compared its value at 98 °C to the value in Fig. 3 from our light scattering results scaled to K_1. The two ratios agree to within 5%, which is well within the measurement errors.

For $T \gtrsim 105$ °C (or $T - T_{NZA} \gtrsim 21$ °C), the ordering $K_3 > K_1 > K_2$ typical of thermotropic nematics holds. As $T \to T_{NZA}$, the splay constant K_1 first gradually decreases (by a factor of 4.5 from $T-T_{NZA} \approx 36$ °C to 6 °C), then turns around and increases within a ~6 °C range above T_{NZA}. Similar behavior – though with a larger decrease preceding the increase – was reported from Freedericksz transition measurements on the pure *trans* DIO stereoisomer.[38] By contrast, in the pure compound RM734 where the AF phase is only ~1 °C wide, K_1 decreases ~7-fold in

a much narrower temperature range above the transition[27] and shows no apparent increase before the transition.

3.2 Relaxation rates and orientational viscosities

To extract relaxation rates of the overdamped fluctuation modes for various scattering angles and temperatures in Geometries 1 and 2, the measured temporal intensity correlation functions were analyzed with the associated electric field correlation function described by a single or double exponential decay – the latter in the Sm Z_A phase at small angles in Geometry 1, where two well-separated decay processes were detected (see examples in Fig. S1).

Fig. 4 plots the temperature-dependent ratios of relaxation rate to squared scattering wavenumber for the same scattering geometries and angles as Fig. 2 and for which a single exponential decay accurately describes the correlation data. In the nematic phase, these correspond to the elasticity to viscosity ratios $\frac{K_1}{\eta_{\text{splay}}}$, $\frac{K_2}{\eta_{\text{twist}}}$, and $\frac{K_3}{\eta_{\text{bend}}}$. The splay, twist and bend viscosities are given by $\eta_{\text{twist}} = \gamma_1$, $\eta_{\text{splay}} = \gamma_1 - \frac{{\alpha_3}^2}{\eta_b}$, and $\eta_{\text{bend}} = \gamma_1 - \frac{{\alpha_2}^2}{\eta_c}$. The twist viscosity γ_1 and the Miesowicz viscosities η_a, η_b, η_c are various combinations of the six Leslie coefficients $\{\alpha_1, \ldots, \alpha_6\}$ characterizing the dissipation in a uniaxial fluid.[36,39]

The relaxation rate for bend (blue points in Fig. 4) decreases slowly and continuously through the nematic to Sm Z_A transition. By contrast, the relaxation rates for splay and twist (orange and green points, respectively) decrease by nearly two orders of magnitude as $T \rightarrow T_{\text{NZA}}$ before abruptly increasing at T_{NZA} roughly back to their nematic levels.

The temperature dependence of the orientational viscosities η_{splay}, η_{twist}, and η_{bend} in the nematic phase, calculated from the results in Fig. 3 and 4, is presented in Fig. 5. The viscosities for splay and twist are nearly equal and increase by an order of magnitude within ~10 °C of T_{NZA}. A similar increase is observed in the compound RM734.[27] The bend viscosity is much lower than the other two viscosities and increases only weakly as $T \rightarrow T_{\text{NZA}}$. Fig. 6 shows the dependence of the dispersion of relaxation rates (Γ *vs.* $\sin^2\theta_s$) measured at T = 90 °C ($T - T_{\text{NZA}}$ = 5.7 °C) in the nematic phase in Geometries 1 and 2. These correspond to the twist-bend normal director mode (denoted n_2 and isolated in Geometry 1) and the splay component of the splay-bend normal mode (denoted n_1 and isolated in Geometry 2). The solid lines are fits to standard expressions for uniaxial nematics,

$$\Gamma_{n_2} = \frac{K_2 q_x^2 + K_3 q_z^2}{\eta_{\text{twist}} - \frac{\alpha_2^2 q_z^2}{\eta_c q_z^2 + \eta_a q_x^2}}$$

and

$$\Gamma_{n_1} = \frac{K_1 (q_x^2 + q_y^2)}{\eta_{\text{splay}}},$$

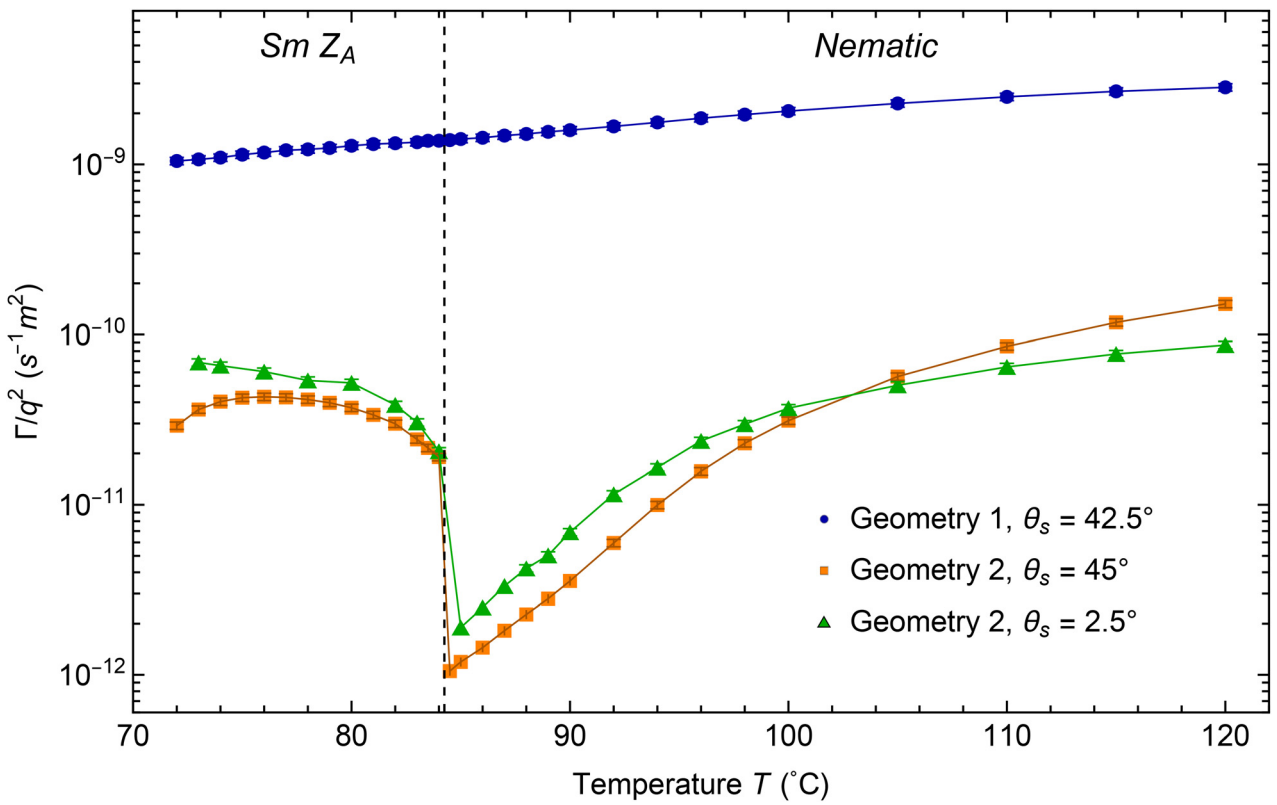

Fig. 4 Ratio of relaxation rates to scattering wavenumber squared *vs.* temperature measured in the same scattering geometries as in Fig. 2. In the nematic phase, the blue, orange, and green points correspond to the ratio of orientational elastic constant to viscosity for pure bend, splay, and twist director fluctuations, respectively. Solid lines are guides to the eye.

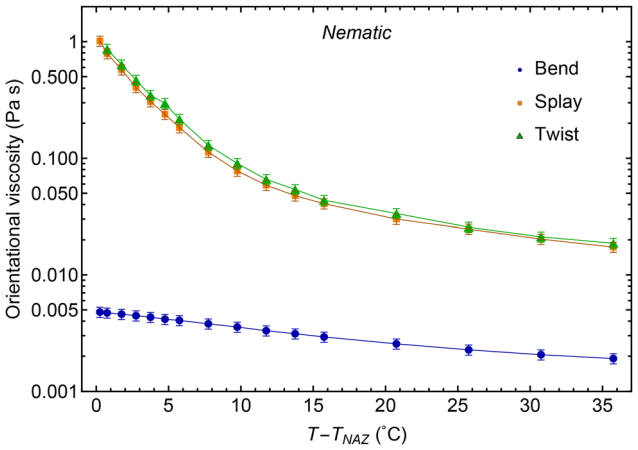

Fig. 5 Orientational viscosities η_{bend}, η_{splay}, η_{twist} in the nematic phase of DIO, plotted *vs.* temperature relative to the nematic to Sm Z_A transition. Solid lines are guides to the eye.

where the components of $\vec{q}$ are calculated from $\sin\theta_s$ and measured $n_\perp$, $n_\parallel$ according to eqn (1). In the fit for Γ_{n_2}, we fixed $\frac{K_3}{\eta_{twist}} = \frac{K_3}{\gamma_1} = 2.9 \times 10^{-11}$ m^2 s^{-1}, $\frac{K_2}{K_3} = 0.24$, and $\frac{\alpha_2^2}{\eta_c\gamma_1} = 1 - \frac{\eta_{bend}}{\eta_{twist}} = 0.98$, which are the values obtained from the results in Fig. 3–5 at $T = 90$ °C ($T - T_{NZA} = 5.7$ °C). Only one parameter, $\frac{\eta_a}{\eta_c}$, was varied, and the fit gives $\frac{\eta_a}{\eta_c} = 0.021$. The solid line for Γ_{n_1} is computed with $\frac{K_1}{\eta_{splay}}$ fixed to the value of $\frac{\Gamma_{n_1}}{q^2} = \frac{K_1}{\eta_{splay}} = 3.7 \times 10^{-12}$ m^2 s^{-1} in Fig. 4 (orange points) at 90 °C.

The standard dynamical theory for a nonpolar uniaxial nematic gives a very good description of the measured dispersion of the relaxation rates in Fig. 6. The large value of the Miesowicz viscosity η_c (for flow with velocity normal to $\hat{n}_0$ and velocity gradient along $\hat{n}_0$) relative to η_a (for flow with both velocity and velocity gradient normal to $\hat{n}_0$) could help explain the fact that both η_{splay} and η_{twist} strongly increase in a parallel fashion as $T \to T_{NZA}$, while η_{bend} shows no pretransitional behavior (Fig. 5). If, in addition to $\eta_c \gg \eta_a$, $\eta_c \sim \gamma_1 \gg \eta_b$ (η_b being the Miesowicz viscosity for flow with velocity and velocity gradient both along $\hat{n}_0$), then the relations $\alpha_3 = \frac{1}{2}(\eta_b - \eta_c + \gamma_1)$ and $\alpha_2 = \frac{1}{2}(\eta_b - \eta_c - \gamma_1)$[36] give $\eta_{splay} = \gamma_1 - \frac{\alpha_3^2}{\eta_b} \approx \gamma_1$ and $\eta_{bend} = \gamma_1 - \frac{\alpha_2^2}{\eta_c} \approx \eta_b$. A large increase in $\eta_{twist} = \gamma_1$ as $T \to T_{NZA}$ therefore also implies the same for η_{splay} but not η_{bend}.

The dispersion of the relaxation rates of director fluctuations in the Sm Z_A phase of DIO differs qualitatively from the results in Fig. 6 for the nematic. As shown in Fig. 7, two distinct relaxation processes are detected in the light scattering correlation function for $\sin^2\theta_s \lesssim 0.1$ in (Geometry 1). Their relaxation rates have opposing dependencies on $\sin^2\theta_s$. In the middle of the Sm Z_A phase, the faster mode increases sharply with decreasing θ_s and intercepts the vertical axis ($\theta_s = 0$) at a large

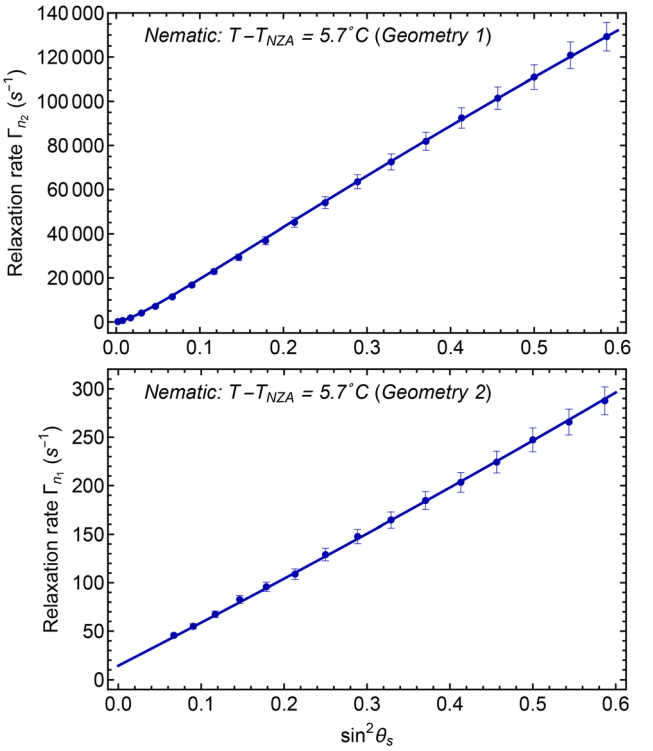

Fig. 6 Dispersion of relaxation rates of the twist-bend director mode (Γ_{n_2}, measured in Geometry 1) and the splay component of the splay-bend mode (Γ_{n_1}, Geometry 2) in the nematic phase of DIO. In the latter case, the scattering at the smallest θ_s studied crosses over to the twist component of the twist-bend mode, and the corresponding points are omitted. Solid lines are fits to the expressions for Γ_{n_2} and Γ_{n_1} given in the text.

value. The intercept decreases substantially at temperatures close to the transitions to the nematic and ferroelectric nematic phases. On the other hand, the slower mode slows down continuously as $\theta_s \to 0$. For $\sin^2\theta_s \gtrsim 0.1$, the two modes apparently coalesce into a single overdamped mode, whose relaxation rate and its dependence on $\sin^2\theta_s$ are similar to the bend mode measured in the nematic phase for the same range of scattering angle.

In Geometry 2, a single overdamped mode is detected below T_{NZA} over the full range of θ_s. However, its relaxation rate *vs.* $\sin^2\theta_s$ is not strictly linear (Fig. 8), as observed in the nematic for the splay component of the splay-bend director mode (Fig. 6).

4 Discussion

As mentioned in the Introduction, different (but not necessarily incompatible) models have been proposed to describe the intermediate, antiferroelectric phase observed in a number of the ferronematic liquid crystals studied so far. Distinct features of these models were inspired by experimental results on different pure compounds or mixtures.

To interpret our light scattering results on DIO, we focus on the smectic-Z_A model. The smectic layer structure implies that elastic moduli for layer compression and tilt relative to the

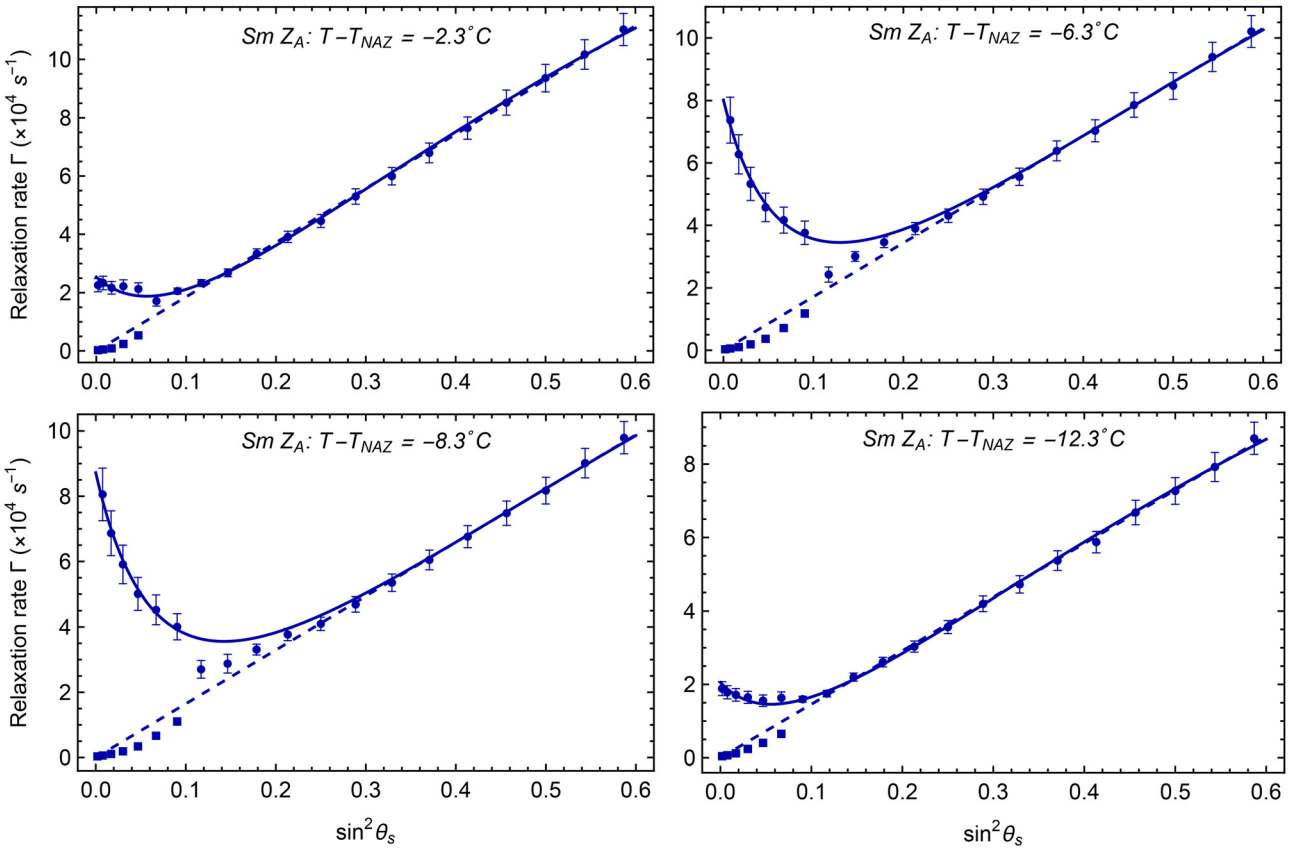

Fig. 7 Dispersion of relaxation rates of overdamped fluctuation modes measured in the Sm Z_A phase of DIO in Geometry 1. For $\sin^2\theta_s \lesssim 0.1$, solid circles and squares correspond to a pair of well-separated modes that contribute to the light-scattering correlation function. For $\sin^2\theta_s \gtrsim 0.1$, the decays of these modes could not be separately resolved, and only a single relaxation rate (also shown by solid circles) was extracted. The solid lines are fits of the higher relaxation rate (solid circles, including the points for $\sin^2\theta_s \gtrsim 0.1$) to the expression in eqn (5) for the relaxation rate of the slower of a pair of coupled layer/director modes in the model described in the text. The dashed lines represent eqn (5) in the limit of no layer/director coupling, where nearly pure bend director fluctuations would dominate at all but the smallest values of θ_s.

director are necessary to describe the long-wavelength fluctuations. It is not sufficient to "coarse-grain" a pure orientational modulation to formulate the elastic free energy density accurately.

As to the question of a one- or two-dimensional splay modulation coexisting with the density modulation, some of our team recently demonstrated[40] that the Sm Z_A phase in DIO, when doped with a chiral additive, develops a Grandjean-type structure with a single twist axis normal to the director and parallel to the direction along which $\vec{P}$ alternates (the layer normal in the smectic-Z_A model). In the case of a 2D splay modulation, the chiral doped phase would not twist along a single direction, since such a twist would either violate equidistance in one of the two modulations or introduce a large number of screw dislocations as grain boundaries between twisted slabs, which were not observed. This result apparently rules out a 2D splay modulation in pure DIO.

In theories that describe splay-modulated AF phases, 1D splay is favored over 2D splay when the modulation period is short.[29] The evidence in DIO of nearly saturated layer polarization and optical birefringence close to that of the uniform nematic[19,20] suggests that amplitude of a splay modulation accompanying the density wave would be quite small. In that case, and given the very short modulation period (~10 nm), the fluctuation modes at optical wavelengths should be reasonably well described by the smectic-Z_A model.

The experimental results cited at the end of Section 2 indicate that the layers form in the bookshelf geometry (Fig. 1) in planar aligned cells, and our results in Fig. 2 are consistent with this orientation. At the high (low) values of θ_s studied in Geometry 2, the scattering is dominated by splay (twist) director fluctuations. In the bookshelf Sm Z_A layer geometry, the corresponding splay (twist) wave vector is parallel (perpendicular) to the layer normal, and the director fluctuations in both cases would be substantially suppressed by the layer structure. That implies a large reduction in scattered intensity at the nematic to Sm Z_A transition, as observed in Fig. 2 for Geometry 2. (On the other hand, if the layers adopted an orientation parallel to the substrate plane, the high (low) angle splay (twist) scattering should remain essentially at the nematic level.)

To investigate the director-layer dynamics of the Sm Z_A phase, we combine an expression for the elastic free energy of a smectic-C (extended to the case of 90° director tilt) with the

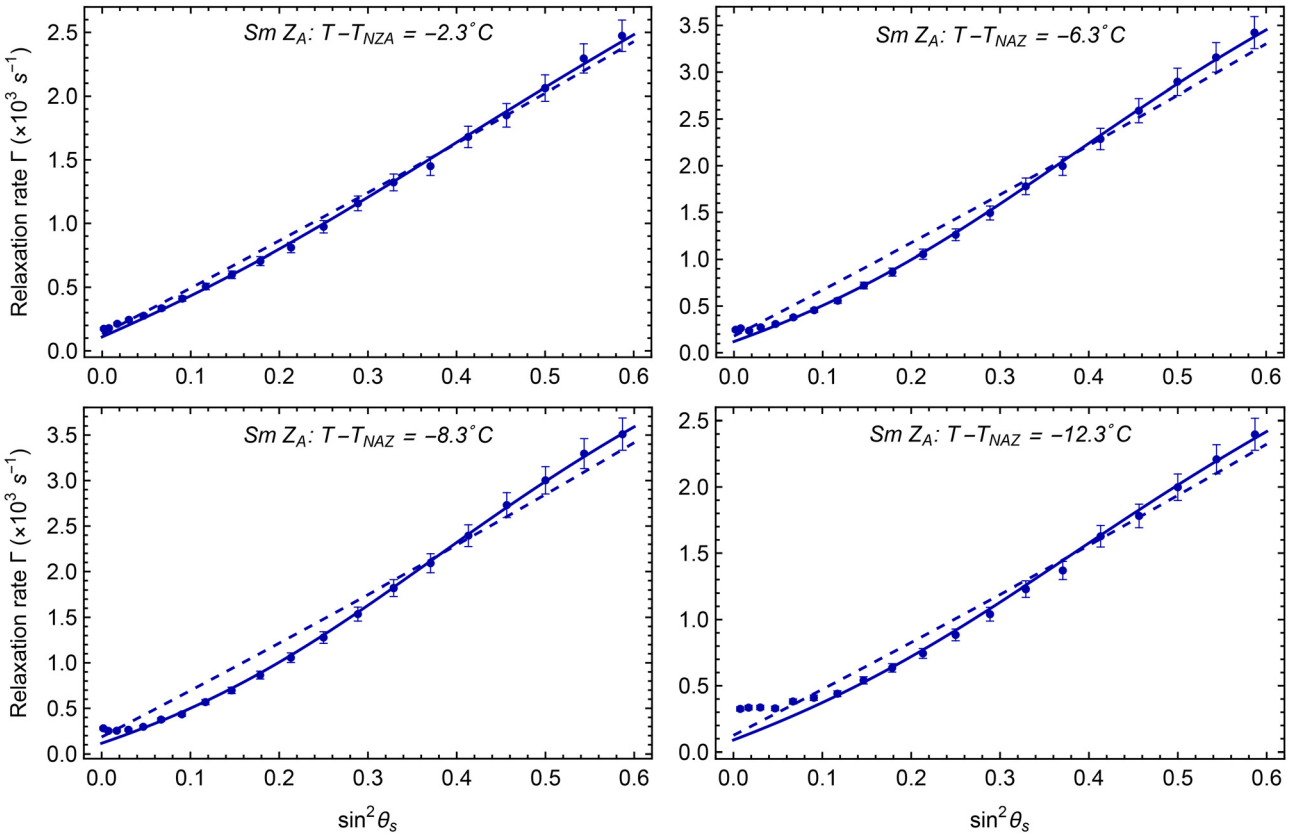

Fig. 8 Dispersion of the relaxation rates of the overdamped fluctuation mode measured in the Sm Z_A phase in Geometry 2. The solid blue lines are fits to eqn (7) for the relaxation rate of the slower of a pair of modes coupling director splay and twist in the model described in the text. The dashed lines are fits to the relaxation rate for pure splay fluctuations in the limit of no coupling.

hydrodynamic equations for an incompressible, uniaxial fluid having negligible inertia (appropriate for the analysis of overdamped fluctuations).

4.1 Elastic free energy density and dynamical equations for the Sm Z_A phase

We consider the rotationally-invariant elastic free energy density of a smectic-C phase presented by Hatwalne and Lubensky.[31] The energy density is the sum of three terms: the usual Frank elastic energy density for small deviations $\delta\hat{n}$ of the uniaxial director from its equilibrium orientation $\hat{n}_0$, a contribution, f_{Sm}, due to the smectic layer structure (with layer displacement denoted by u), and a term $f_{\hat{N}}$ that is quadratic in rotationally invariant derivatives of the layer orientation specified by layer normal $\hat{N}$.

To quadratic order in the variation, $\delta q_s = -\vec{q}_0\cdot\nabla u$, of the smectic layering wavenumber q_s from its equilibrium value q_0 and variations $\delta\Phi$ of the director tilt angle Φ from its equilibrium value Φ_0, Hatwalne and Lubensky obtain

$$f_{Sm} = \frac{1}{2}B[\hat{q}_0\cdot\nabla u + c\delta\Phi]^2 + \frac{1}{2}D(\delta\Phi)^2.$$

The coefficients $B = \frac{1}{q_0^2}\left(\frac{\partial^2 f_{Sm}(q_s,\cos\Phi_0)}{\partial q_s^2}\right)_{q_s=q_0(\cos\Phi_0)}$ and $D = \left(\frac{\partial^2 f_{Sm}(q_0,(\cos\Phi),\cos\Phi)}{\partial\Phi^2}\right)_{\Phi=\Phi_0}$ are smectic elastic moduli that correspond to layer compression and layer tilt relative to the director, respectively. They vanish in the absence of smectic order. The parameter c is given by $c = \frac{1}{q_0}\left(\frac{\partial q_0(\cos\Phi)}{\partial\Phi}\right)_{\Phi=\Phi_0}$ where $q_0(\cos\Phi)$ is the value of q_s that minimizes f_{Sm} for a given value of $\cos\Phi$. (Thus, $q_0(\cos\Phi_0) \equiv q_0 = \frac{2\pi}{d_0}$, where d_0 is the equilibrium layer spacing.)

Note that $\delta(\cos\Phi) = -\sin\Phi_0\delta\Phi = \delta(\hat{n}\cdot\hat{N}) = \hat{N}_0\cdot\delta\hat{n} + \hat{n}_0\cdot\delta\hat{N}$ and $\delta\hat{N} = -[\nabla - \hat{q}_0(\hat{q}_0\cdot\nabla)]u$ to linear order in the variations. Then, since $\Phi_0 = \frac{\pi}{2}$ and $\hat{n}_0\cdot\hat{q}_0 = 0$ for Sm Z_A layers, we get $\hat{n}_0\cdot\delta\hat{N} = \hat{n}_0\cdot\nabla u$ and $\delta\Phi = \hat{q}_0\cdot\delta\hat{n} + \hat{n}_0\cdot\nabla u$. Also, in the Sm Z_A case, the coefficient c is zero in the expression for f_{Sm} above for the following reason: By symmetry, $q_0(\cos(\pi/2 + \delta\Phi)) = q_0(\cos(\pi/2 - \delta\Phi))$, which, assuming $\frac{\partial q_0(\cos\Phi)}{\partial\Phi}$ is continuous, implies $\frac{\partial q_0(\cos(\pi/2+\delta\Phi))}{\partial\delta\Phi} = 0$ or $\left(\frac{\partial q_0(\cos\Phi)}{\partial\Phi}\right)_{\Phi=\Phi_0} = 0$ for $\Phi_0 = \pi/2$.

We may use these results to write f_{Sm} in terms of $\delta\hat{n}$ and u for the limiting case of Sm Z_A layer structure. Including the Frank energy density for the uniaxial director and taking the simplest form for the free energy density associated with gradients in

layer orientation, $f_{\hat{N}} = \frac{1}{2}K_u(\nabla \cdot \delta\hat{N})^2 = \frac{1}{2}K_u\left[\left(\nabla^2 - (\hat{q}_0 \cdot \nabla)^2\right)u\right]^2$ where K_u is an elastic constant for layer curvature, we arrive at the following form for the elastic free energy density,

$$\begin{aligned} f_{\mathrm{SmZ}} &= \frac{1}{2}K_1(\nabla \cdot \delta\hat{n})^2 + \frac{1}{2}K_2[\hat{n}_0 \cdot (\nabla \times \delta\hat{n})]^2 \\ &+ \frac{1}{2}K_3[\hat{n}_0 \times (\nabla \times \delta\hat{n})]^2 + \frac{1}{2}B(\hat{q}_0 \cdot \nabla u)^2 \\ &+ \frac{1}{2}K_u\left[\left(\nabla^2 - (\hat{q}_0 \cdot \nabla)^2\right)u\right]^2 + \frac{1}{2}D(\hat{q}_0 \cdot \delta\hat{n} - \hat{n}_0 \cdot \nabla u)^2, \end{aligned}$$

to quadratic order in $\delta\hat{n}$ and u.

f_{SmZ} has a form similar to the elastic energy density for a smectic-A phase, but the term that couples director deformations to gradients in the layer displacement differs significantly. In the Sm A, the coupling is isotropic in the layer plane, whereas in the Sm Z_A only gradients in u along a single direction in the layer plane (the direction $\hat{n}_0$) couple to director distortions (specifically to the component of $\hat{n}$ along the layer normal), up to quadratic order.

We next take the Fourier transform of f_{SmZ} and express the transformed $\delta\hat{n}$ as $\delta\hat{n} = n_1\hat{e}_1 + n_2\hat{e}_2$, where $\hat{e}_2 = \frac{\hat{n}_0 \times \vec{q}_\perp}{q_\perp}$, $\hat{e}_1 = \hat{e}_2 \times \hat{n}_0$ are orthogonal unit vectors in the plane normal to $\hat{n}_0$ and $\vec{q}_\perp$ is the projection of the fluctuation wave vector $\vec{q}$ into this plane. The components n_1 and n_2 correspond to the usual splay-bend and twist-bend director modes in a uniaxial nematic. The result for f_{SmZ} in $\vec{q}$ space is

$$\begin{aligned} f_{\mathrm{SmZ}} &= \frac{1}{2}\left(K_1 q_\perp^2 + K_3 q_\parallel^2\right)|n_1|^2 + \frac{1}{2}\left(K_2 q_\perp^2 + K_3 q_\parallel^2\right)|n_2|^2 \\ &+ \frac{1}{2}B(\hat{q}_0 \cdot \vec{q})^2|u|^2 + \frac{1}{2}K_u\left[q^2 - (\hat{q}_0 \cdot \vec{q})^2\right]^2|u|^2 \\ &+ \frac{1}{2}D\left|\frac{\hat{q}_0 \cdot \vec{q}_\perp}{q_\perp}n_1 + \frac{\hat{q}_0 \cdot (\hat{n}_0 \times \vec{q}_\perp)}{q_\perp}n_2 - iq_\parallel u\right|^2. \end{aligned} \quad (2)$$

where $q_\parallel = \hat{n}_0 \cdot \vec{q}$. In the nematic phase, $B = D = K_u = 0$ and eqn (2) reduces to the elastic free energy of a uniaxial nematic with normal director modes n_1 (splay-bend) and n_2 (twist-bend).

For the two scattering geometries in Fig. 1, we may obtain dynamical equations for the fluctuating variables n_1, n_2, and u from the basic hydrodynamic theory for an incompressible smectic (see Appendix) and f_{SmZ} in eqn (2).

4.1.1 Geometry 1: $\hat{n}_0 \parallel$ scattering plane. The scattering vector in Geometry 1 (Fig. 1a) is $\vec{q} = q_x\hat{x} + q_z\hat{z}$. Then, for layers strictly vertical to the cell surfaces in the bookshelf geometry, $\hat{q}_0$ is normal to the x–z plane, so $\hat{q}_0 \cdot \vec{q} = 0$ and the layer compression term in f_{SmZ} drops out.

However, X-ray diffraction[19] reveals that as DIO is cooled below T_{NZA}, the layer spacing contracts from initial value d_0 to $d < d_0$. To fill the same volume, the layers buckle, and in thin DIO samples confined between substrates treated for planar director alignment, the buckling produces a chevron layer structure shown schematically in Fig. 9. The chevron angle, $\delta = \cos^{-1}(d/d_0)$, reaches a maximum of $\sim 10^\circ$ (0.17 rad) in the middle of the Sm Z_A phase. The optical texture of the chevron structure in DIO and DIO-containing mixtures[19,20] – namely "zig-zag" defect lines that delineate interfaces between oppositely-pointing chevron domains – resembles the classical texture observed in smectics-C. Our light scattering cell also showed isolated "zig-zag" lines (Fig. S3(d)) separating relatively large, uniform chevron domains.

Referring to Fig. 9, the layer normal is given by $\hat{q}_0 = \sin\delta\hat{x} + \cos\delta\hat{y}$ in the presence of the chevron structure, and $\hat{q}_0 \cdot \vec{q} = \sin\delta q_x \approx \delta q_x$. The layer compression term in eqn (2) then contributes to f_{SmZ} and to the dynamics studied in Geometry 1. Also, using the coordinates in Fig. 1a, $n_0 = \hat{z}$, $q_\parallel = q_z$, and $\vec{q}_\perp = q_x\hat{x}$, so $\hat{q}_0 \cdot \vec{q}_\perp \approx \delta q_x$ and $\hat{q}_0 \cdot (\hat{n}_0 \times \hat{q}_0) \approx 1$ in the last term in eqn (2). Thus, for nonzero δ, splay-bend director fluctuations (n_1) couple to both twist-bend (n_2) and layer displacement (u) fluctuations.

From eqn (2) and eqn (A1)–(A4) in the Appendix, and for small δ, we obtain the following dynamical equations in Geometry 1

$$\eta(\vec{q})\frac{\partial n_1}{\partial t} + \left(K_1 q_x^2 + K_3 q_z^2\right)n_1 + D\delta(n_2 - iq_z u + \delta n_1) = 0 \quad (3a)$$

$$\eta_{\mathrm{twist}}\frac{\partial n_2}{\partial t} + \left(K_2 q_x^2 + K_3 q_z^2\right)n_2 + D(n_2 - iq_z u + \delta n_1) + i\alpha_2 q_z\frac{\partial u}{\partial t} = 0 \quad (3b)$$

$$\begin{aligned} &\left(q_x^2\eta_a + q_z^2\eta_c\right)\frac{\partial u}{\partial t} + \left(B\delta^2 q_x^2 + K_u q_\perp^4\right)u \\ &+ iDq_z(n_2 - iq_z u + \delta n_1) - i\alpha_2 q_z\frac{\partial n_2}{\partial t} = 0. \end{aligned} \quad (3c)$$

The viscosity $\eta(\vec{q})$ (whose detailed form will not be needed) has

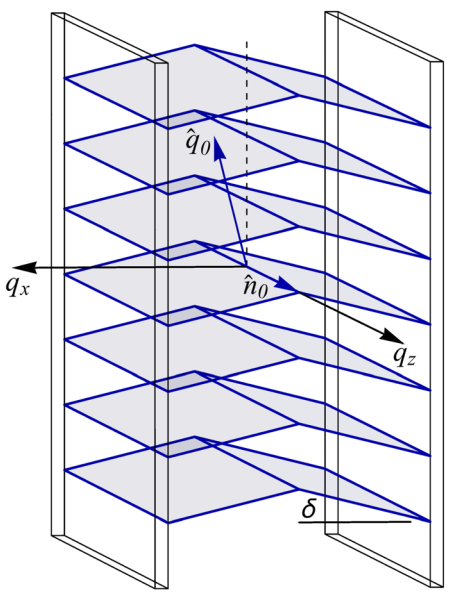

Fig. 9 Schematic of chevron layer structure in a section of a Sm Z_A sample initially formed in the "bookshelf" geometry. The wave vector $\vec{q}_0$ describing the smectic density wave is tilted with respect to the substrate planes by the chevron angle $\pm\delta$. The average director ($\hat{n}_0$) remains parallel to the layer and substrate planes. The components of the scattering vector are shown for Geometry 1, where $\vec{q}$ lies in the x–z plane.

limiting values η_{splay} when $q_z = 0$ ($\theta_s = 0$) and η_{bend} when $q_z^2 \gg q_x^2$ (large θ_s).

The relaxation rates Γ of the normal modes may be obtained by putting n_1, n_2, $u \propto \exp(-\Gamma t)$ in eqn (3) and solving the resulting system of linear equations. We consider the strong coupling limit, where $D \gg (B\delta^2, K_\alpha q^2)$ and therefore $n_2 - iq_z u + \delta n_1 \approx 0$, and the limit $\delta \ll 1$. In this case, the normal modes consist of two slower ("hydrodynamic") modes, one coupling layer curvature to director bend (relaxation rate $\Gamma^-_{n_2,u}$) and the other representing splay-bend of the director within the layer planes (relaxation rate Γ_{n_1}), plus a fast ("nonhydrodynamic") mode involving tilt of the director out of the layer plane (relaxation rate $\Gamma^+_{n_2,u}$). $\Gamma^+_{n_2,u}$ has a gap at $\vec{q} = 0$ proportional to D. For the slower hydrodynamic modes, we find

$$\Gamma_{n_1} \approx \frac{1}{\eta(\vec{q})}\left(K_1 q_x^2 + K_3 q_z^2\right) \tag{4}$$

$$\Gamma^-_{n_2,u} \approx \frac{B\delta^2 q_x^2 + K_u\left(q_x^2 + q_z^2\right)^2 + K_2 q_x^2 q_z^2 + K_3 q_z^4}{\eta_a q_x^2 + \eta_b q_z^2} \tag{5}$$

where $\eta_b = 2\alpha_2 + \gamma_1 + \eta_c$. The Miesowicz viscosities η_b and η_a in eqn (5) correspond to shear flows associated with Sm Z_A layer sliding.

4.1.2 Geometry 2: $\hat{n}_0 \perp$ scattering plane. In Geometry 2 (Fig. 1b), $\hat{n}_0 = \hat{z}$ and $\vec{q} = \vec{q}_\perp$ with $q_\parallel = 0$. The coupling of layer displacement u to n_1 and n_2 drops out in f_{SmZ} (eqn (2)). For small δ, $\vec{q} \approx q_x\hat{x} + q_y\hat{y}$ and the dynamical equations for n_1, n_2 are

$$\eta_{splay}\frac{\partial n_1}{\partial t} + \left(K_1 q_\perp^2 + D\frac{q_y^2}{q_\perp^2}\right)n_1 + D\frac{q_x q_y}{q_\perp^2}n_2 = 0 \tag{6a}$$

$$\eta_{twist}\frac{\partial n_2}{\partial t} + \left(K_2 q_\perp^2 + D\frac{q_x^2}{q_\perp^2}\right)n_2 + D\frac{q_x q_y}{q_\perp^2}n_1 = 0. \tag{6b}$$

In the large D limit, the normal modes are strongly coupled combinations of n_1 and n_2. The relaxation rate $\left(\Gamma^-_{n_1,n_2}\right)$ of the faster mode again has a gap proportional to D. For the slower, hydrodynamic mode, we obtain

$$\Gamma^-_{n_1,n_2} \approx \frac{\left(K_1 q_x^2 + K_2 q_y^2\right)q_\perp^2}{\eta_{splay} q_x^2 + \eta_{twist} q_y^2}. \tag{7}$$

The chevron structure sketched in Fig. 9 is symmetric about the mid-plane of the cell. Because the layer rotation does not impose a director reorientation in the case of a Sm Z_A phase, each half of the chevron structure contributes the same scattering intensity from director fluctuations, the same degree of coupling between layer displacement and director fluctuations, and the same normal mode relaxation rates in eqn (5) and (7). This result should also apply in the case of asymmetric chevrons, where the chevron interface is displaced from the cell mid-plane, or to a uniformly tilted bookshelf layer geometry (with layers tilted by angle δ from the substrate normal).

4.2 Comparison of the model to experimental results

4.2.1 For Geometry 1. The solid blue curves in Fig. 7 are fits of the relaxation rate of the faster mode detected in Geometry 1 to the expression for $\Gamma^-_{n_2,u}$ in eqn (5) after substituting eqn (1) and utilizing measured values of the refractive indices $n_\perp$, $n_\parallel$. The fits include the data for $\sin^2\theta_s \geq 0.1$, where only a single decay could be resolved in the light scattering correlation function. The fit quality was insensitive to the twist contribution, so we set $K_2 = 0$. We also neglected the term in K_u since the inverse scattering intensity for bend is practically continuous across $T = T_{NZA}$ (Fig. 2), implying $K_u \ll K_3$. The parameter K_3/η_b was constrained to ±10% of the slope of the data in Fig. 7 for $\sin^2\theta \geq 0.4$. In this regime, $q_z^2 \gg q_x^2$, and (neglecting K_u) eqn (5) reduces to $\Gamma^-_{n_2,u} \approx \dfrac{K_3 q_z^2}{\eta_b}$, which is linear in $\sin^2\theta_s$. Thus, only two parameters, $B\delta^2/\eta_b$ and η_a/η_b, were freely varied at each temperature.

The fits give a reasonably good description of the data, except for values of $\sin^2\theta_s \sim 0.15$ where the light scattering correlation function crosses over from a double to single exponential decay. For reference, the dashed lines in Fig. 7 represent the limit of no layer/director coupling, $D \to 0$. In that limit, $\Gamma^-_{n_2,u}$ reduces to Γ_{n_2} given in Section III.B for the twist-bend director mode, which is dominated by bend over most of the range of $\sin^2\theta_s$.

The model for $\Gamma^-_{n_2,u}$ and the results in Fig. 7 indicate that the parameter $B\delta^2$ is largest at temperatures in the middle of the Sm Z_A phase, which is consistent with the X-ray scattering results in ref. 19 that show the layer shrinkage and chevron angle δ are maximal within this range. From the fit for $T - T_{NAZ} = -8.3$ °C, we find $B\delta^2/K_3 = 1.6 \times 10^{14}$ m^{-2}. Since bend fluctuations are hardly affected by the Sm Z_A layer structure (see Fig. 2 and 4), we may extrapolate from the nematic phase to obtain $K_3 = 7.0 \times 10^{-12}$ N and therefore $B\delta^2 = 1.1 \times 10^3$ N m^{-2}. Then, using $\delta \approx 10^\circ$ (0.17 rad),[19] we estimate the layer compression constant to be $B \approx 3.8 \times 10^4$ N m^{-2}.

Because we do not have a direct measurement of δ in our sample, the value of B should be regarded as an order of magnitude estimate that is ~100 times smaller than in a typical calamitic smectic-A liquid crystal.[41] Evidently, the Sm Z_A layer structure is considerably softer than a conventional Sm A.

The chevron layer structure implies a contribution from splay-bend fluctuations within the layers (the n_1 mode) to the scattering in Geometry 1, which accounts for detection of the slower relaxation rate at small θ_s in Fig. 7. In Fig. 1a, the scattering and layer planes coincide in the undistorted bookshelf geometry ($\delta = 0$). Then, for the n_1 mode, both $\hat{n}_0$ and $\delta\hat{n}$ lie in the scattering plane and there is no component along the incident light polarization, which is normal to the scattering plane in Geometry 1. However, if $\delta \neq 0$, the layer planes incline with respect to the scattering plane, and n_1 fluctuations have a small component along the incident polarization. This component contributes significantly at low θ_s (low q) where the amplitude of n_1 is large.

According to eqn (1) and (4), Γ_{n_1} crosses over from $\dfrac{K_1 q_x^2}{\eta_{splay}}$ to $\dfrac{K_3 q_z^2}{\eta_{bend}}$ with increasing θ_s. Then, provided $\eta_{bend} \sim \eta_b$, Γ_{n_1} and

$\Gamma^{-}_{n_2,u}$ have similar magnitude and q dependence for large θ_s. This would explain why the measured correlation function evolves to a single exponential decay at high angles, which is dominated by director bend on both sides of T_{NZA}. That, in turn, explains the continuity of ${I_n}^{-1}$ and $\frac{\Gamma}{q^2}$ at the transition observed in Fig. 2 and 4 for $\theta_s = 42.5^\circ$ in Geometry 1.

4.2.2 For Geometry 2. As described in Section IV.A, splay and twist fluctuations studied in in Geometry 2 are coupled due to the layer structure. Only one of the coupled modes is "slow"; its relaxation rate $\Gamma^{-}_{n_1,n_2}$ (eqn (7)) vanishes as $\vec{q} \to 0$.

At low scattering angle, where $q_y \to 0$, $\Gamma^{-}_{n_1,n_2}$ reduces to $\frac{K_1 {q_x}^2}{\eta_{splay}}$, which describes splay fluctuations with wave vector parallel to the layer planes ($\hat{x}$ direction in Fig. 1b). The corresponding scattering amplitude is expected to be weak both because the selection rule for splay scattering is small at low angle in Geometry 2 and because the energy cost of splay and the effective K_1 are presumably enhanced due to the polarization field in each layer. At large angles where $q_x \to 0$ (eqn (1)), $\Gamma^{-}_{n_1,n_2} \approx \frac{K_2 {q_y}^2}{\eta_{twist}}$ and the slower mode is dominated by twist fluctuations with wave vector nearly normal to the layers ($\hat{y}$ direction in Fig. 1b). However, the selection rule for twist scattering is very small for larger θ_s (specifically, $\theta_s \sim 40^\circ$). The development of Sm Z_A layer structure therefore explains the strong decrease in scattering intensity (or increase in its inverse) that we observe below the nematic phase for both high and low θ_s studied in Geometry 2 (see Fig. 2).

In the Sm Z_A phase, with $\hat{n}_0$ parallel to the layers, pretransitional fluctuations of the smectic order produce a resistance to director splay, stiffening K_1. On the other hand, flexoelectric coupling of the director to polar order fluctuations in the nematic phase softens K_1. Competition between these effects could explain the non-monotonic temperature dependence of K_1 in Fig. 3.

The Sm Z_A layer structure with temperature-dependent chevron angle δ also accounts for the dip in inverse scattering intensities observed in Geometry 2 on cooling below the transition. When δ is nonzero, the scattering selection rules admit greater depolarized scattering from the splay component of the slower (n_1, n_2) mode at small θ_s and from the twist component at large θ_s. The enhancement of scattered intensity in both cases is proportional to δ^2. Thus, a dip and local minimum in inverse intensity would arise from an increase in δ, followed by a decrease, as the temperature is lowered through the Sm Z_A phase. Such a temperature-dependent δ agrees with the results from the X-ray diffraction measurements in ref. 19.

We modeled the relaxation rate data in Fig. 8 using eqn (7) for $\Gamma^{-}_{n_1,n_2}$, which applies when n_1 and n_2 are strongly coupled. We also fit the data to $\Gamma_{n_1} = \frac{K_1 {q_x}^2}{\eta_{splay}}$, which applies for weak coupling ($D \to 0$) where n_1 fluctuations dominate the scattering selection rule, except at very small θ_s.

The results are shown by the solid and dashed lines in Fig. 8. Measured values of $n_\perp$, $n_\parallel$ were used to calculate $\vec{q}$ according to eqn (1). For Γ_{n_1}, K_1/η_{splay} was varied. For $\Gamma^{-}_{n_1,n_2}$, we additionally varied the parameters K_2/η_{splay} and $\eta_{splay}/\eta_{twist}$. The weak coupling model (dashed lines) is clearly inadequate. On the other hand, eqn (7) describes the data reasonably well for $\sin\theta_s \gtrsim 0.1$; however, it undershoots the points at small θ_s and lower temperature.

One possible explanation for the undershoot comes from considering the impact of polarization splay that accompanies the director splay. In equilibrium, the polarization field is uniform over macroscopic scales within each Sm Z_A layer but alternates with nanoscale period along the layer normal. Splay of $\vec{P}$ incurs an electrostatic energy penalty due the accumulation of polarization charge, $\rho_P = -\vec{\nabla}\cdot\delta\vec{P} = -P_0\vec{\nabla}\cdot\delta\vec{n}$, which may be partially screened by mobile impurity ions. In the Debye model with screening length ξ, the effective splay energy density is:[42] $K_1^{eff} {q_\perp}^2 {n_1}^2 = \left(K_1 + \frac{{P_0}^2}{\varepsilon_0\varepsilon_\perp\left({q_\perp}^2 + \xi^{-2}\right)}\right){q_\perp}^2{n_1}^2$, where $\varepsilon_\perp$ is the dielectric constant for electric displacement normal to the director. If ${q_\perp}^2 \ll \xi(\phi)^{-2}$ (reasonable for optical $\vec{q}$ and small θ_s), then K_1 is replaced by $K_1^{eff} \approx K_1 + \frac{{P_0}^2\xi^2}{\varepsilon_0\varepsilon_\perp}$, but the $\vec{q}$ dependence is unchanged in eqn (7).

On the other hand, if we consider an anisotropic screening length that varies as $\xi(\phi)^2 = {\xi_1}^2\sin^2\phi + {\xi_2}^2\cos^2\phi = {\xi_2}^2 + ({\xi_1}^2 - {\xi_2}^2)\sin^2\phi$, where ϕ is the angle from the Sm Z_A layer normal around $\hat{n}_0$ and toward the layer plane, we obtain an anisotropic form for the effective splay elastic energy density, given (to lowest order in chevron angle δ) by:

$$\left[\left(K_1 + \frac{{P_0}^2{\xi_2}^2}{\varepsilon_0\varepsilon_p}\right){q_\perp}^2 + \frac{{P_0}^2\left({\xi_1}^2 - {\xi_2}^2\right)}{\varepsilon_0\varepsilon_\perp}{q_x}^2\right]{n_1}^2 \equiv \left(K_1^{eff}{q_\perp}^2 + \Delta K {q_x}^2\right){n_1}^2.$$

Replacing $K_1{q_\perp}^2$ in Eqn (7) with $K_1^{eff}{q_\perp}^2 + \Delta K {q_x}^2$ then yields

$$\Gamma^{-}_{n_1,n_2} = \frac{\left(K_1^{eff}{q_x}^2 + K_2{q_y}^2\right){q_\perp}^2 + \Delta K {q_x}^4}{\eta_{splay}{q_y}^2 + \eta_{twist}{q_y}^2}$$

The screening length for polarization charge produced by long wavelength splay could be limited in the direction normal to the Sm Z_A layers by the periodic reversal of $\vec{P}$ and $\vec{\nabla}\cdot\vec{P}$ along this direction, resulting in $\xi_2 < \xi_1$. That condition, in turn, results in an increase in $\Gamma^{-}_{n_1,n_2}$ selectively for small θ_s, exactly what is needed to better match the data in Fig. 8. However, it also introduces another variable parameter and given the speculation involved, we will not pursue further quantitative analysis here.

The fits of the relaxation rate data in Fig. 8 to eqn (7) yield large ratios of splay to twist elastic constants and viscosities – namely, $\frac{K_1}{K_2} \sim 10$ and $\frac{\eta_{splay}}{\eta_{twist}} \sim 15$ in the middle of the Sm Z_A range. Due to large fitting uncertainties, particularly for the viscosity ratio, these results should be considered as order of magnitude estimates. The large $\frac{\eta_{splay}}{\eta_{twist}}$ is inconsistent with the standard hydrodynamic theory for a uniaxial fluid, which

requires $\frac{\eta_{splay}}{\eta_{twist}} \leq 1$.[36] Perhaps additional term(s) in the dissipative stress allowed by the layer polarization or coupling to slow diffusion of screening ions could account for such a large damping of splay fluctuations.

Finally, we compare the relaxation rate $\Gamma^{-}_{n_1,n_2}$ in Fig. 8 with Γ_{n_1} for the slower mode in Fig. 7 in the limit $\theta_s \to 0$. According to eqn (4) and (7), in this limit both should correspond to splay fluctuations with wavevector $q \approx q_x$ parallel to the layers. At each temperature, the values (extrapolated from the low-angle data) agree within 10%.

5. Conclusions

We reported a dynamic light scattering study on the paraelectric nematic and antiferroelectric smectic-Z_A phases in the liquid crystal DIO. With decreasing temperature in the nematic phase, we observe a softening of the splay elastic constant followed by an increase just above the transition to the Sm Z_A phase. The twist and bend elasticities slowly increase with decreasing temperature, exhibiting no remarkable pretransitional behavior. On the other hand, both the splay and twist viscosities show very large pretransitional enhancements.

We developed a dynamical theory to explain the temperature dependence of the scattered light intensity and the dispersion of relaxation rates of the fluctuation modes observed in the Sm Z_A phase. The theory is based on three ingredients: an extension of the elastic free energy for a smectic-C to the case of 90° director tilt from the layer normal; the approximation of the dissipative stress by the form derived for an incompressible, uniaxial fluid; and incorporation of the effect of a chevron layer structure caused by temperature-dependent layer shrinkage, which was identified in previous experimental studies on DIO.

Our experimental results are generally well described by the theory. Quantitative analysis of the relaxation rate for coupled layer displacement/director bend fluctuations yields an estimate of the layer compression modulus in the Sm Z_A phase that is two orders of magnitude lower than in a conventional Sm *A* liquid crystal. However, the theory falls short in accounting for the dispersion of coupled splay/twist director fluctuations at low wave numbers, and it yields an anomalous ratio of splay to twist viscosity. These issues warrant further effort to improve the model. Particularly useful would be light scattering measurements to explore the fluctuation modes in a Sm Z_A sample with layers parallel to the substrate planes; such a geometry can be produced by application and subsequent removal of a low frequency in-plane electric field.[19]

It would also be interesting to perform comparative studies of the fluctuation modes in other compounds and mixtures that possess an intermediate phase between the *para*- and ferroelectric nematic states, whether identified as Sm Z_A, splay-modulated in one or two dimensions, or an entirely new type.

Conflicts of interest

There are no conflicts to declare.

Data availability

Data will be made available upon reasonable request.

Supplementary information (SI) is available. See DOI: https://doi.org/10.1039/d5sm00796h.

Appendix

We consider a one-dimensional smectic density wave along the direction $\hat{q}_0$, neglect permeation of molecules between layers, and assume the system is incompressible. After spatial Fourier transformation, the hydrodynamic equations may be written as[36,43]

$$\rho\frac{d\vec{v}}{dt} = i\vec{q}\cdot\vec{\vec{\sigma}}' - \frac{\delta f_Z}{\delta u} - i\left(\vec{q}\cdot\vec{\vec{\sigma}}'\cdot\vec{q}\right)\frac{\vec{q}}{q^2} + q_y\frac{\delta f_Z}{\delta u}\frac{\vec{q}}{q^2} \tag{A1}$$

$$\frac{\delta f_Z}{\delta n_\alpha} = -h_\alpha \tag{A2}$$

with

$$\frac{\partial u}{\partial t} = \hat{q}_0\cdot\vec{v} \tag{A3}$$

and

$$\vec{q}\cdot\vec{v} = 0 \tag{A4}$$

Here ρ is the mass density, $\vec{v}$, u, and n_α are the Fourier transforms of the velocity, layer displacement, and fluctuating components of the director; $\vec{\vec{\sigma}}'$ is the Fourier transform of the dissipative stress tensor; f_{SmZ} is given by eqn (2) in the text; and $\vec{h}$ is the Fourier transform of the "molecular field" or force conjugate to rate of change of the director relative to the background fluid. In the hydrodynamic theory, the components $\sigma'_{\alpha\beta}$ and h_α are linear combinations of spatial derivatives of the velocity and time derivatives of the director. After Fourier transform, these components may be expressed in the n_1, n_2 basis defined in Section IVA. The last two terms on the right side of eqn (A1) enforce the incompressibility condition, eqn (A4).

To obtain eqn (3) and (6) of the main text, we drop the inertial term $\rho\frac{d\vec{v}}{dt}$ on the left side of eqn (A1), as is appropriate to describe the overdamped fluctuations measured experimentally, and we assume that the forms of $\vec{\vec{\sigma}}'$ and $\vec{h}$ from the standard hydrodynamic theory for a uniaxial fluid[39] are applicable (*i.e.*, biaxiality of the Sm Z_A phase can be neglected).

Acknowledgements

The research reported here was supported by the National Science Foundation under grants no. DMR-2210083 (AG, PG, RT, JG, AJ, SS) and DMR-2341830 (BB, HW, ODL).

References

1 H. Nishikawa, K. Shiroshita, H. Higuchi, Y. Okumura, Y. Haseba, S. I. Yamamato, K. Sago and H. A. Kikuchi, *Adv. Mater.*, 2017, **29**, 1702354.
2 R. J. Mandle, S. J. Cowling and J. W. Goodby, *Phys. Chem. Chem. Phys.*, 2017, **19**, 11429–11435.
3 R. J. Mandle, S. J. Cowling and J. W. Goodby, *Chem. – Eur. J.*, 2017, **23**, 14554–14562.
4 X. Chen, E. Korblova, D. Dong, X. Wei, R. Shao, L. Radzihovsky, M. A. Glaser, J. E. Maclennan, D. Bedrov, D. M. Walba and N. A. Clark, *Proc. Natl. Acad. Sci. U. S. A.*, 2020, **117**, 14021–14031.
5 M. Born, *Sitzungsber. Preuss. Akad Wiss.*, 1916, **30**, 614–650.
6 R. Mandle, N. Sebastian, J. Martinez-Perdiguero and A. Mertelj, *Nat. Commun.*, 2021, **12**, 4962.
7 R. J. Mandle, *Soft Matter*, 2022, **18**, 5014–5020.
8 X. Chen, Z. Zhu, M. J. Magrini, E. Korblova, C. S. Park, M. A. Glaser, J. E. Maclennan, D. M. Walba and N. A. Clark, *Liq. Cryst.*, 2022, **49**, 1531–1544.
9 R. Saha, P. Nepal, C. Feng, M. S. Hossain, M. Fukuto, R. Li, J. T. Gleeson, S. Sprunt, R. J. Twieg and A. Jákli, *Liq. Cryst.*, 2022, **49**, 1784–1796.
10 E. Cruikshank, *ChemPlusChem*, 2024, **89**, e202300726.
11 A. Adaka, P. Guragain, K. Perera, P. Nepal, B. Almatani, S. Sprunt, J. Gleeson, R. J. Twieg and A. Jákli, *Liq. Cryst.*, 2024, **51**, 1140–1148.
12 J. Li, H. Nishikawa, J. Kougo, J. Zhou, S. Dai, W. Tang, X. Zhao, Y. Hisai, M. Huang and S. Aya, *Sci. Adv.*, 2021, **7**, eab5047.
13 A. Manabe, M. Bremer and M. Kraska, *Liq. Cryst.*, 2021, **48**, 1079–1086.
14 Y. Song, J. Li, R. Xia, H. Xu, X. Zhang, H. Lei, W. Peng, S. Dai, S. Aya and M. Huang, *Phys. Chem. Chem. Phys.*, 2022, **24**, 11536–11543.
15 Y. Arakawa, Q. Ning, S. Karthick and S. Aya, *J. Mater. Chem. C*, 2024, **12**, 16206–16217.
16 K. Perera, R. Saha, P. Nepal, R. Dharmarathna, M. S. Hossain, M. Mostafa, A. Adaka, R. Waroquet, R. J. Twieg and A. Jákli, *Soft Matter*, 2023, **19**, 347–354.
17 S. Brown, E. Cruickshank, J. M. D. Storey, C. T. Imrie, D. Pociecha, M. Majewska, A. Makal and E. Gorecka, *ChemPhysChem*, 2021, **22**, 2506–2510.
18 X. Chen, V. Martinez, P. Nacke, E. Korblova, A. Manabe, M. Klasen-Memmer, G. Freychet, M. Zhernenkov, M. A. Glaser, L. Radzihovsky, J. E. Maclennan, D. M. Walba, M. Bremer, F. Giesselmann and N. A. Clark, *Proc. Natl. Acad. Sci. U. S. A.*, 2022, **119**, e2210062119.
19 X. Chen, V. Martinez, E. Korblova, G. Freychet, M. Zhernenkov, M. A. Glaser, C. Wang, C. Zhu, L. Radzihovsky, J. E. Maclennan, D. M. Walba and N. A. Clark, *Proc. Natl. Acad. Sci. U. S. A.*, 2023, **120**, e2217150120.
20 P. Nacke, A. Manabe, M. Klasen-Memmer, X. Chen, V. Martinez, G. Freychet, M. Zhernenkov, J. E. Maclennan, N. A. Clark, M. Bremer and F. Giesselmann, *Sci. Rep.*, 2024, **14**, 4473.
21 J. Karcz, J. Herman, N. Rychlowicz, P. Kula, E. Gorecka, J. Szydlowska, P. W. Majewski and D. Pociecha, *Science*, 2024, **384**, 1096–1099.
22 H. Nishikawa, D. Okada, D. Kwaria, A. Nihonyanagi, M. Kuwayama, M. Hoshino and F. Araoka, *Adv. Sci.*, 2024, **11**, 2405718.
23 G. J. Strachan, E. Górecka, J. Szydlowska, A. Makal and D. Pociecha, *Adv. Sci.*, 2024, 2409754.
24 Y. Song, S. Aya and M. Huang, *Giant*, 2024, **19**, 100318.
25 T. P. Rieker, N. A. Clark, G. S. Smith, D. S. Parmar, E. B. Sirota and C. R. Safinya, *Phys. Rev. Lett.*, 1987, **59**, 2658–2661.
26 P. M. Rupnik, E. Hanžel, M. Lovšin, N. Osterman, C. J. Gibb, R. J. Mandle, N. Sebastián and A. Mertelj, *Adv. Sci.*, 2025, e2414818.
27 A. Mertelj, L. Cmok, N. Sebastian, R. J. Mandle, R. R. Parker, A. C. Whitwood, J. W. Goodby and M. Copic, *Phys. Rev. X*, 2018, **8**, 041025.
28 Z. Ma, M. Jiang, A. Sun, S. Yi, J. Yang, M. Huang, S. Aya and Q.-H. Wei, *Phys. Rev. Lett.*, 2025, **134**, 238101.
29 M. P. Rosseto and J. V. Selinger, *Phys. Rev. E*, 2020, **101**, 052707.
30 A. V. Emelyanenko, V. Y. Rudyak, S. A. Shvetsov, F. Araoka, H. Nishikawa and K. Ishikawa, *Phys. Rev. E*, 2024, **109**, 014701.
31 Y. Hatwalne and T. C. Lubensky, *Phys. Rev. E: Stat. Phys., Plasmas, Fluids, Relat. Interdiscip. Top.*, 1995, **52**, 6240–6249.
32 H. Nishikawa, K. Sano, S. Kurihara, G. Watanabe, A. Nihonyanagi, B. Dhara and F. Araoka, *Commun. Mater.*, 2022, **3**, 89.
33 P. Nacke, R. Tuffin, M. Klasen-Memmer, P. Rudquist and F. Giesselmann, *Sci. Rep.*, 2024, **14**, 15018.
34 K. Thapa and O. D. Lavrentovich, unpublished.
35 P. Kumari, B. Basnet, M. O. Lavrentovich and O. D. Lavrentovich, *Science*, 2024, **383**, 1364–1368.
36 P. G. de Gennes and J. Prost, *The Physics of Liquid Crystals*, Clarendon Press, Oxford, 2nd edn, 1993.
37 J. T. Gleeson, S. N. Sprunt, A. Jákli, P. Guragain and R. J. Twieg, *Soft Matter*, 2025, **21**, 5862–5870.
38 J. Zhou, R. Xia, M. Huang and S. Aya, *J. Mater. Chem. C*, 2022, **10**, 8762–8766.
39 F. M. Leslie, *Adv. Liq. Cryst.*, 1979, **4**, 1–81.
40 K. Thapa, O. S. Iadlovska, B. Basnet, H. Wang, A. Paul, J. T. Gleeson and O. D. Lavrentovich, *Phys. Rev. E*, 2024, **109**, 054702.
41 M. Benzekri, J. P. Marcerou, H. T. Nguyen and J. C. Rouillon, *Phys. Rev. B: Condens. Matter Mater. Phys.*, 1990, **41**, 9032.
42 E. Zavvou, M. Klasen-Memmer, A. Manabe, M. Bremer and A. Eremin, *Soft Matter*, 2022, **18**, 8804.
43 G. d'Etude des Cristaux Liquides (Orsay), *J. Chem. Phys.*, 1969, **51**, 816–822.

